Journal of Materials Chemistry C

ROYAL SOCIETY OF CHEMISTRY

PAPER

View Article Online
View Journal | View Issue

Cite this: J. Mater. Chem. C, 2024, 12, 9595

A $NaBiF_4$:Gd/Tb nanoscintillator for high-resolution X-ray imaging†

Manisha Bungla,[ab] Mohit Tyagi,[c] Ashok K. Ganguli *[bd] and Paras N. Prasad *[a]

Received 15th April 2024,
Accepted 7th May 2024

DOI: 10.1039/d4tc01543f

rsc.li/materials-c

Lanthanide doped fluoride nanoscintillators have received tremendous attention due to their high photochemical stability and tunable X-ray excited optical luminescence compared to traditional inorganic scintillators. Advancement in this field requires design strategies for the development of nanoscintillators that offer tailorable excitation dynamics through nanostructuring, thus enabling high luminescence in a suitable host. However, selection of an appropriate host matrix with low phonon energy and a nanoarchitecture that mitigates surface quenching due to the large surface-to-volume ratio of nanoparticles is still a challenge. Herein, we introduce $NaBiF_4$:Gd,Tb (NBF) nanoparticles as highly efficient nanoscintillators with reduced afterglow to minimize interference in radioimaging, which utilizes the high X-ray attenuation coefficient of bismuth (5.74 cm^2 g^{-1} at about 100 keV). The host $NaBiF_4$ has a high refractive index and low phonon energy, which reduces the multiphonon non-radiative relaxation rates and enhances the radiative emission probability, thus yielding a long-life time for luminescence. Furthermore, by varying the composition of the nanoparticles and the relative concentrations of Gd and Tb, luminescence at multiple wavelengths in changing relative intensities can be achieved to enable multiplexed imaging. We show that $NaBiF_4$:Gd/Tb can be easily synthesized using the co-precipitation method at room temperature within 1 min. Furthermore, we succeeded in fabricating organic–inorganic nanocomposite self-standing films of $NaBiF_4$:Gd,Tb in high loading, uniformly dispersed in poly(methyl methacrylate) (PMMA) polymer. Their application in radiography is demonstrated by recording X-ray images using a commercially available charge-coupled device camera. We attained a resolution comparable to the non-flexible commercial CsI (Tl) scintillator and significantly superior to the commercial Gd_2O_2S:Tb, GOS:Tb scintillators commonly used for screens.

1. Introduction

Scintillators act as an energy transformer, converting high-energy X-rays into low energy visible or ultraviolet photons.[1–3] These are broadly employed to actualize X-ray excited optical luminescence (XEOL) imaging in security inspections and industrial materials[4–6] as well as in medical imaging[7–9] and space explorations.[10,11] Conventional scintillators (for example: NaI:Tl,[12] $Lu_3Al_5O_{12}$:Ce[13] and $Bi_4Ge_3O_{12}$[14]) have been successfully developed and applied to a variety of commercial X-ray detectors. However, these traditional inorganic scintillators are typically confined to bulk crystals, and exhibit uncontrollable particle sizes,[15,16] non-uniform morphology,[17] non-tunable XEOL wavelength,[18,19] and limited conversion efficiency, hindering their practical utility.[20,21] As a result, it would be critical to investigate innovative methods for developing highly efficient and cost-effective scintillators[22,23] to overcome the aforementioned constraints and fulfil the rising needs of X-ray imaging technologies.

Lanthanide-doped fluoride nanoscintillators have received tremendous attention due to their high photochemical stability[24–28] and tunable X-ray excited optical luminescence[29,30] compared to the traditional inorganic scintillators. However, the limited availability and high cost of rare earth compounds restricts the commercialization of these scintillator materials.[31–33] As a consequence, development of less expensive and non-rare earth and environmentally friendly host materials for scintillators is required urgently. Fortunately, elements like bismuth can substitute the rare earth element in $NaREF_4$-based matrices with comparable performance.[34,35] The advancements in this field demand the development of nanoscintillators with tailorable excitation

[a] Department of Chemistry and The Institute for Lasers, Photonics and Biophotonics, University at Buffalo (SUNY), 14260 Buffalo, NY, USA. E-mail: pnprasad@buffalo.edu
[b] Department of Chemistry, Indian Institute of Technology Delhi, Hauz Khas, New Delhi 110016, India. E-mail: ashok@chemistry.iitd.ac.in
[c] Technical Physics Division, Bhabha Atomic Research Centre, Trombay, Mumbai 400085, India
[d] Department of Chemical Sciences, Indian Institute of Science Education & Research, Laudigam, Berhampur, Odisha 760003, India

† Electronic supplementary information (ESI) available: Elemental mapping, EDX spectrum, PLE, PL spectrum, XEOL spectra, persistent luminescence decay curve and radioluminescence stability of NBF:20Gd/20Tb powder samples. See DOI: https://doi.org/10.1039/d4tc01543f

dynamics through effective nanostructuring, facilitating high luminescence within a suitable host matrix. However, a significant research gap persists in the selection of an appropriate host matrix with low phonon energy and a nanoarchitecture that mitigates surface quenching, a consequence of the large surface-to-volume ratio in nanoparticles.

Herein, we introduce $NaBiF_4$:Gd,Tb (NBF) nanoparticles as a highly efficient nanoscintillator with reduced afterglow to minimize interference in radioimaging. Interest in bismuth-based compounds arises as these phosphors are an intriguing class of optical materials with the additional benefit of being intrinsically suitable for multi-imaging due to the high X-ray attenuation coefficient of bismuth (5.74 cm^2 g^{-1} at about 100 keV).[36–40] $NaBiF_4$ has a high refractive index and low phonon energy, which reduces the multiphonon non-radiative relaxation rates and enhances the radiative emission probability.[41,42] Apart from this, $NaBiF_4$ can be easily synthesized at room temperature within 1 min.[43] However, to date, the scintillation properties and X-ray imaging of lanthanide-doped $NaBiF_4$ NSs are rarely reported. These promising features motivated us to further investigate bismuth based compounds as luminescent materials/scintillators.

In this work, we report room temperature synthesis of $NaBiF_4$:Gd/Tb as an inorganic scintillator with strong radioluminescence (RL) performance and weak afterglow. Furthermore, we succeeded in fabricating organic–inorganic nanocomposite self-standing films of $NaBiF_4$:Gd,Tb with high loading, uniformly dispersed in a poly(methyl methacrylate) (PMMA) polymer matrix. The novel nanocomposite films, thus developed, hold significant promise for applications in radiography. The research showcases their efficacy by recording X-ray images using a commercially available charge-coupled device (CCD) camera. The achieved resolution is not only comparable to the non-flexible commercial CsI (Tl) scintillator but also significantly superior to the widely used Gd_2O_2S:Tb^{40} and GOS:Tb^{41} scintillators employed in commercial screens. By addressing the research gap in host matrix selection and nanoarchitecture design, this study contributes to the advancement of lanthanide-doped fluoride nanoscintillators, paving the way for their enhanced performance and broader application in X-ray imaging technologies.

2. Experimental

2.1 Materials

Bismuth nitrate pentahydrate (CDH, >99%), sodium nitrate (Fisher Scientific), and ammonium fluoride (Qualigens fine Chemicals) were used. Terbium(III) nitrate pentahydrate ($Tb(NO_3)_3{\cdot}5H_2O$, 99.9%) and gadolinium(III) nitrate hexahydrate ($Gd(NO_3)_3{\cdot}6H_2O$, 99.99%) were purchased from Sigma-Aldrich. Ethylene glycol and toluene were obtained from Thermo Fisher Scientific India Pvt. Ltd. Polymethyl methacrylate (PMMA) was purchased from Tokyo Chemical Industry Co., Ltd. CsI (TI) commercial scintillator was purchased from Fermi mechanical and electrical equipment company. All chemicals were used as such without any further purification.

2.2 Synthesis of $NaBiF_4$:Tb^{3+}

$NaBiF_4$:Tb^{3+} nanoparticles were synthesized using the chemical precipitation method. To synthesize $NaBiF_4$:x%Tb^{3+} (x = 2, 6, 10, 12, 16, 20, 24, 30), $Bi(NO_3)_3{\cdot}5H_2O$ ($(1-x)$ mmol), $Tb(NO_3)_3{\cdot}5H_2O$ (x = 0.02, 0.06, 0.1, 0.12, 0.16, 0.20, 0.24 and 0.30 mmol) was dissolved in 10 mL of EG. In another flask, 14 mmol of NH_4F was dissolved in 20 mL of ethylene glycol with magnetic stirring. These two solutions were mixed together at room temperature and allowed to stir for 30 min. The solution became milky after 10 s, which indicates the formation of nanoparticles. The solution was centrifuged at 3000 rpm to obtain a white precipitate, which was further washed with ethanol. The precipitate was dried overnight in an oven at 65 °C.

2.3 Preparation of a thin film

First, 100 mg PMMA and 1 mL toluene solution were mixed and stirred to form a transparent solution. After that NBF:Gd,Tb nanoparticles were added into PMMA toluene solution, and stirred for more than 3 hours until the solution was uniform paste-like and did not agglomerate. These solutions were deposited on a quartz substrate by using a spin coater. Then, these solutions were spin coated on quartz slides at 1000 rpm for 20 s and kept for drying at room temperature for 2 h.

Characterization. Powder X-ray diffraction measurements were carried on a Bruker D8 Advance diffractometer with Cu Kα radiation, λ = 0.154178 nm, within a 2θ range of 10–80°. The size and surface morphology of all the samples were examined using a high resolution JEOL JSM-7800F Prime Field Emission Scanning Electron Microscope. In addition to this, a high-resolution transmission electron microscope (Tecnai G2 20, 200 kV) was used for TEM images. For PL measurements, a QuantaMaster 8450-22 (Horiba) 450-watt Xenon lamp for photoluminescence and a 60-watt Xe Flash lamp for phosphorescence were used for excitation. The X-ray excited radioluminescence (RL), measurements were carried out using a customized Seifert X-ray generator with a W tube operating at 40 kV and 30 mA. The RL emission was recorded with the help of an optical fiber-based Avamatsu spectrometer.

3. Results and discussion

The X-ray diffraction (XRD) patterns revealed that all the resulting NBF:Ln NPs belonged to the hexagonal phase and no impurity peaks were observed (Fig. 1(a) and (b)).

Fig. S1 (ESI†) depicts the PXRD pattern of the nanoparticles formed immediately after turbidity appearance, which matches with the hexagonal phase of $NaBiF_4$. The PXRD pattern of the nanoparticles formed after 1 min of reaction matches well with the nanoparticles obtained after 30 min of reaction; hence, it confirms the formation of $NaBiF_4$ immediately after mixing the solutions.

However, compared with the standard PDF card (PDF #41-0796), as the doping of Tb^{3+} concentration increases from 2% to 30% for NBF:x%Tb and from 0.5% to 25% for NBF:20% Gd,x%Tb, the positions of the diffraction peaks shift to large

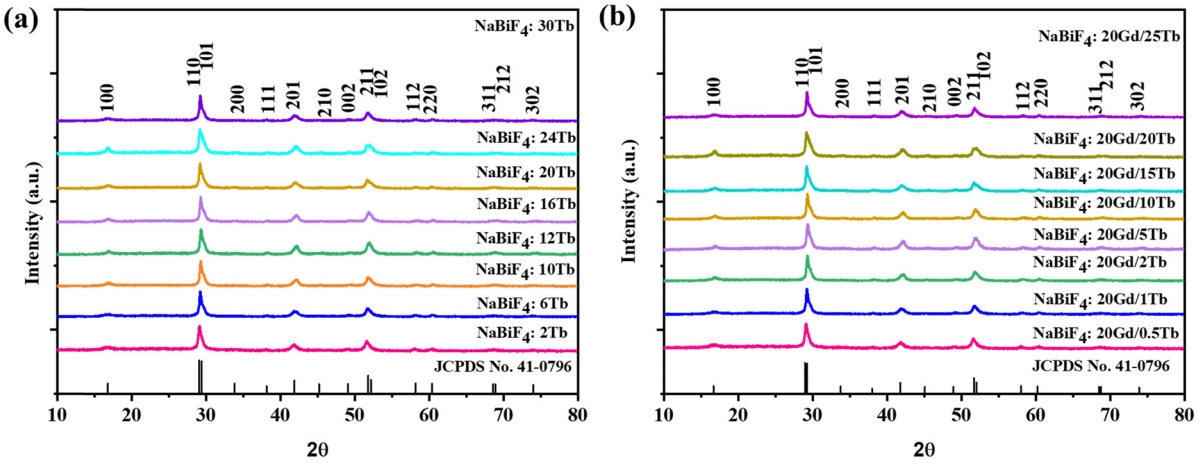

Fig. 1 Powder XRD patterns of (a) NBF:*x*%Tb and (b) NBF:20%Gd,*x*%Tb.

angles, which is caused by the decrease of the interplanar spacing (d). Since the radii of Tb^{3+} ions and Gd^{3+} ions are slightly smaller than the radius of Bi^{3+} ions, the substitution of Tb^{3+} ions and Gd^{3+} ions for Bi^{3+} ions causes lattice shrinkage (and hence the interplanar spacings), which further suggests that the rare-earth ions successfully occupy the lattice site of Bi^{3+}. The peak observed around 41° of these patterns is magnified and shown in Fig. S2 (ESI†). It is clearly seen that the peak is shifting toward higher 2θ with increasing Tb^{3+} concentration. This is attributed to lattice shrinkage due to replacement of larger Bi^{3+} ions with smaller Tb^{3+} and Gd^{3+} ions as mentioned earlier. To confirm this fact, these XRD patterns are analysed by the Rietveld refinement method and the refinement plots are shown in Fig. S3 (ESI†). The refined unit cell parameters, typical structural parameters and residuals of the refinements are given in Table S1 (ESI†).

Moreover, when the dopant concentration increases from 2% to 24%, the XRD patterns of the samples remain in good agreement with those for hexagonal $NaBiF_4$ nanocrystals.

Scanning electron microscopy (SEM) (Fig. 2(a)) and transmission electron microscopy (TEM) micrographs (Fig. 2(b)) indicate that the synthesized NPs exhibit a spherical shape. High-resolution TEM images show clear lattice fringes with a d-spacing of 0.305 nm corresponding to the (110) plane (Fig. 2(c)). The presence of Na, Bi, Gd, Tb, and F elements in the NPs was confirmed by energy-dispersive X-ray (EDX) spectra [Fig. S4(g), ESI†], and elemental mapping images [Fig. S4(a)–(f) and S4(b), ESI†] indicated a uniform distribution of these elements.

Gd/Tb co-doped systems have been broadly used to realize UV-excited downshifted emission, in which the input UV photons are absorbed by Gd^{3+} sensitizers and then transferred to Tb^{3+} activators. A high doping concentration of activators allows the harvesting of photon energy *via* energy transfer during UV excitation, but it also causes detrimental cross-relaxation and energy migration to surface quenchers. In our experimental results, we found that the optical characteristics between the UV-excited downshifted emission and the XEOL emission were significantly different.

Emission spectra from the NBF:*x*%Tb nanoparticles (with varying concentrations of Tb) upon excitation at 376 nm are shown in Fig. 3(a). With the excitation of 376 nm UV light, NBF:*x*%Tb shows several narrow emission bands mainly in the green and orange part of the visible region due to the typical $^5D_4$–$^7F_5$ (J = 3, 4, 5, and 6) transition of the Tb^{3+} ion. The emission spectrum consists of four sharp peaks at 490, 544, 590 and 621 nm and is attributed to the $^5D_4 \rightarrow {}^7F_6$, $^5D_4 \rightarrow {}^7F_5$, $^5D_4 \rightarrow {}^7F_4$, and $^5D_4 \rightarrow {}^7F_3$, transitions, respectively due to the Tb^{3+} ions present in the NBF lattice.[42] These emission bands are dominated by the emission originating at 544 nm from the $^5D_4 \rightarrow {}^7F_5$ transition. The optimal doping content of Tb^{3+} ions

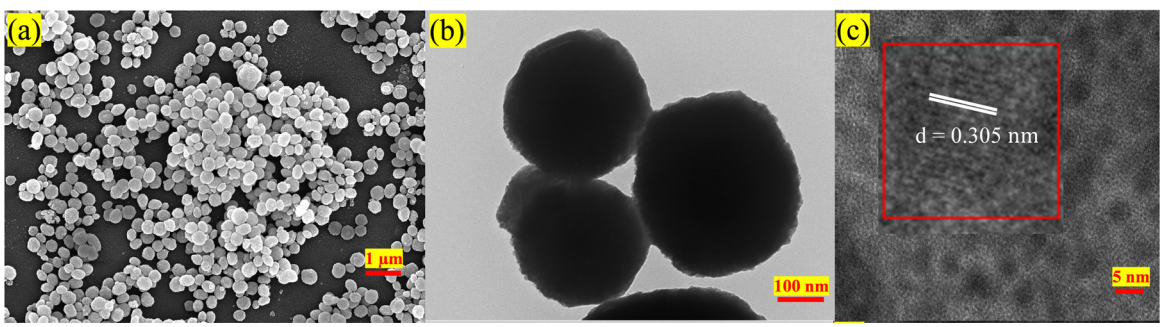

Fig. 2 (a) FE-SEM, (b) TEM and (c) HRTEM images of the NBF:Gd,Tb nanoparticles.

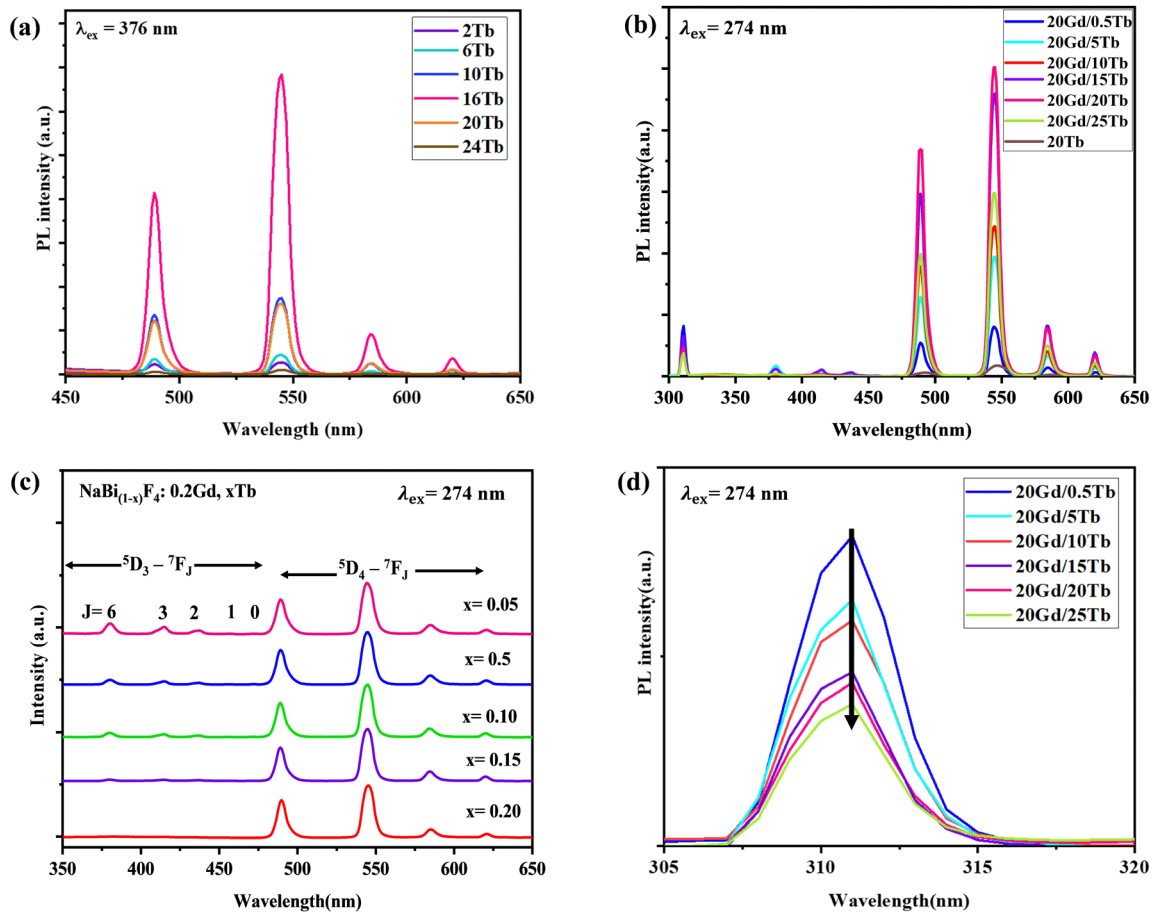

Fig. 3 (a) PL spectra of NBF:*x*%Tb (*x* = 2–24%) under 376 nm excitation; (b) and (c) NBF:20Gd,*x*%Tb under 273 nm excitation; (d) PL emission spectra from Gd^{3+} ions corresponding to emission at 310 nm.

was only about 16 mol% and the emission intensity was enhanced about ~3.8 times compared with that of 10 mol%. Integrated PL intensity profiles at various Tb^{3+} doping contents are shown in Fig. S5 (ESI†). The decrease in emission intensity beyond 16 mol% is attributed to concentration quenching. The radioluminescence spectrum of NBF:*x*%Tb and NBF:Gd,Tb nanoparticles upon X-ray excitation was recorded, as shown in Fig. 4(a) and (b). However, in the case of XEOL, the optimum doping concentration of Tb^{3+} ions was 24 mol% (Fig. 4(a)) and the XEOL intensity was enhanced by 3 times when increasing

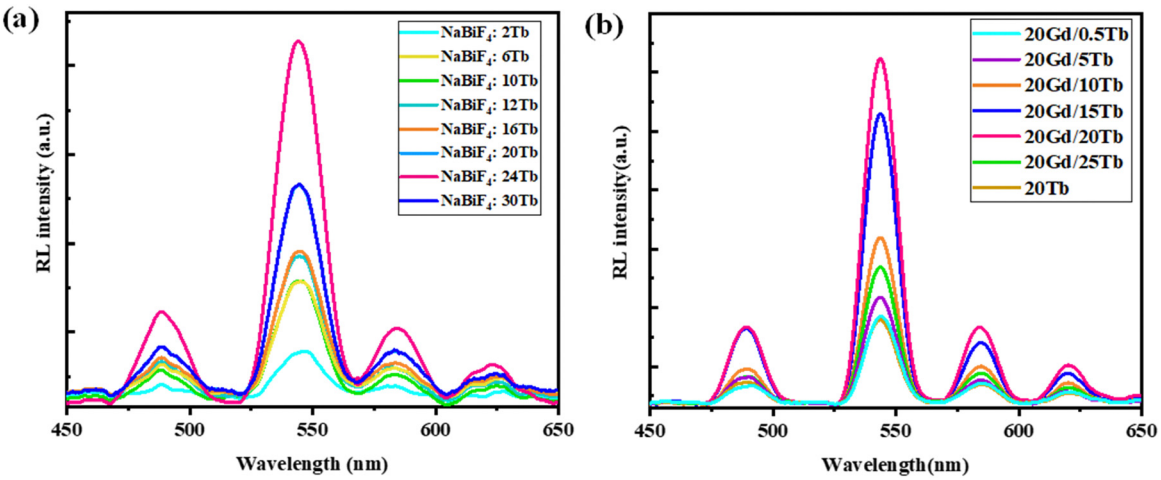

Fig. 4 (a) RL spectra of NBF:Tb and (b) NBF:20%Gd,Tb (*x* = 0.5–25%) nanoparticles.

the Tb^{3+} ion dopant concentration from 2% to 24 mol%; then it started to decrease with a further increase in the Tb^{3+} ion dopant concentration to 30 mol%. According to the PL decay curves, the 16 mol% Tb^{3+} doped sample had a longer lifetime than the 12 and 20 mol% samples (Fig. 5(a)), supporting the efficient contribution due to radiative transition. The photoluminescence excitation spectra (Fig. S6, ESI†) of NBF:Gd,Tb correspond to 544 nm emission and consist of a sharp peak with a maximum at ~274 nm along with less intense peaks. Peaks at about 273 and 312 nm are assigned to the Gd^{3+} transitions from the ground level $^8S_{7/2}$ to excited levels ^6I_J, ^6P_J, respectively. Narrow peaks above 300 nm are assigned to intra-configurational f–f transitions of Tb^{3+} ions, *i.e.*, $^7F_6 \rightarrow {}^5D_{0,1}$ (317, 327 nm), $^7F_6 \rightarrow {}^5G_{2-6}$ (341, 350, 357 nm) and $^7F_6 \rightarrow {}^5D_{2,3}$ (368, 377 nm) transitions.

To further investigate the energy transfer from Gd^{3+} to Tb^{3+} ions, the emission spectrum of NBF:20Gd^{3+},xTb^{3+} ($0.5\% \leq x \leq 25\%$) monitored at 274 nm was measured, as shown in Fig. 3(b)–(d). The emissions could be attributed to $^5D_3 \rightarrow {}^7F_J$ (J = 2, 3, 4, 5 and 6) and $^5D_4 \rightarrow {}^7F_J$ (J = 3, 4, 5 and 6) transitions of Tb^{3+} ions, among which the transition $^5D_4 \rightarrow {}^7F_5$ leads to green emission at 544 nm. The $^5D_4$ emission of Tb^{3+} increased, while the $^5D_3$ emission decreased with an increase in the Tb^{3+} content, which is due to the cross relaxation between the $^5D_3 \rightarrow {}^5D_4$ transition and $^7F_6 \rightarrow {}^7F_0$ transition of Tb^{3+}. The $^5D_4$ emission of Tb^{3+} increased rapidly with an increase in the concentration of Tb^{3+}. This is due to numerous factors along with the cross relaxation between the $^5D_3$ and $^5D_4$ levels since luminescence centres increase with the concentration of the Tb^{3+} ions in the host. The decreasing emission intensities from Gd^{3+} ions at 310 nm (Fig. 3(d)) with increasing Tb^{3+} ion content indicated that much more efficient energy transfer from Gd^{3+} to Tb^{3+} ions occurs in a sample. The highest PL intensity was observed for NBF:20Gd,20Tb nanoparticles. The PL decay curves suggested that the NBF:20Gd,20Tb sample exhibited a longer lifetime than that of NBF:20Tb, which confirms the efficient energy transfer from Gd^{3+} to Tb^{3+} ions [Fig. 5(a) and (b)].

Nonetheless, in our experimental results, the optical characteristics between the UV-excited downshifted emission and the XEOL emission were significantly different. The energy capture and transfer mechanisms were investigated to explain the different optical luminescence intensity variation trends under UV and X-ray excitation.

The proposed mechanism of X-ray scintillation in the lanthanide doped nanoscintillators is described below. The incident X-ray photons (<50 keV) first interact with all heavy elements present (Bi^{3+}, Gd^{3+}, and Tb^{3+}) to generate hot electrons and deep holes, mainly through the photoelectric effect and the Compton scattering effect (Fig. 6). Subsequently, a large number of secondary electrons are produced *via* electron–electron scattering and the Auger process, resulting in the creation of charge carriers with significantly lower kinetic energy. These numerous charge carriers, including electrons and holes, are predominantly directed towards luminescence centers. To understand the process of electron population in the excited states of Tb^{3+}, X-ray-excited optical luminescence (XEOL) intensities were measured for NBF:20Tb and NBF:20Gd/20Tb NPs under identical conditions. In comparison to NBF:20Tb nanoparticles, the XEOL intensity increased after doping with Gd^{3+} ions, as depicted in Fig. 4(b). This suggests that the Gd^{3+} $^6P_{7/2}$ state has the ability to capture a portion of the secondary electrons and then transfer the energy to Tb^{3+}:$^5D_3$ states to produce strong green emission upon X-ray radiation. The maximum XEOL intensity was seen in NBF:20Gd/20Tb and is also in accordance with the PL results (Scheme 1).

A significant decrease in the luminescence persistence was observed and this is due to the generation of fluoride vacancies and interstitials as electron traps (E-traps) and hole traps (H-traps) due to elastic collisions between X-ray photons and fluoride ions. The captured secondary electrons in E-traps migrate to the conduction band and subsequently to activators, leading to radiative emission through electron–hole recombination. Compared to $NaBiF_4$:24Tb, the afterglow was significantly quenched with doping Gd^{3+} (20 mol%) and Bi^{3+} (60 mol%) ions (Fig. S7, ESI†), confirming that both Gd^{3+} and Bi^{3+} ions could quench the afterglow. Owing to the elastic collision of large momentum X-ray photons with small fluoride ions, fluoride vacancies and interstitials are formed as electron

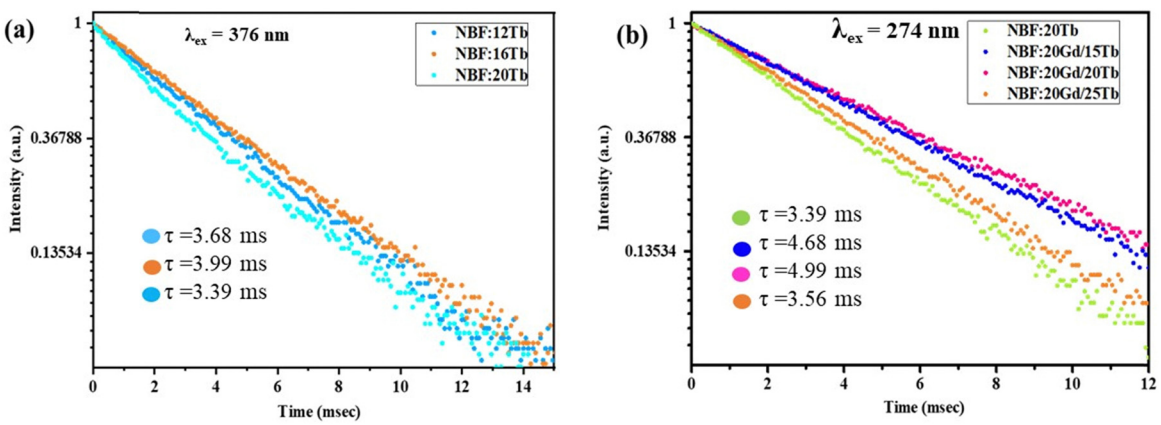

Fig. 5 (a) PL decay curves of NBF:xTb and (b) NBF:20%Gd,x%Tb (x = 15, 20, 25) nanoparticles.

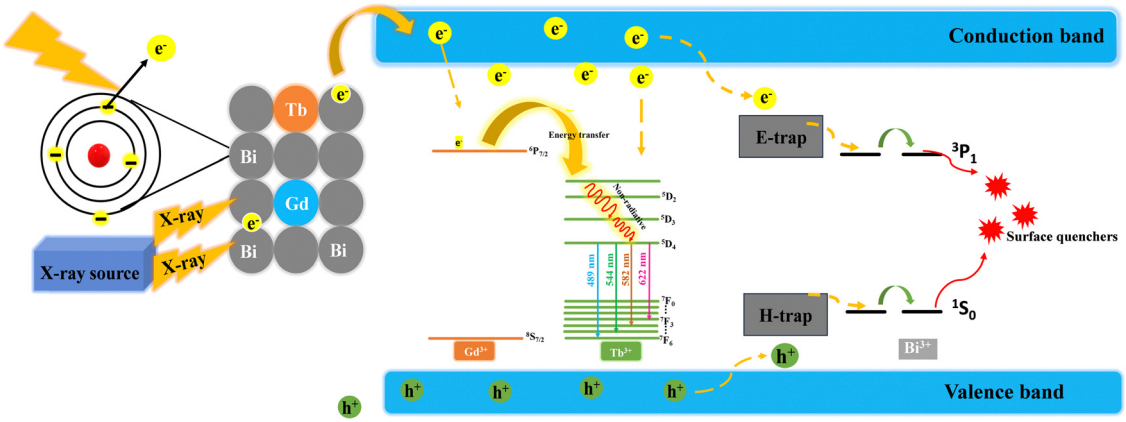

Fig. 6 Proposed energy conversion and transport and luminescence mechanisms in the NBF:Gd/Tb nanoscintillator.

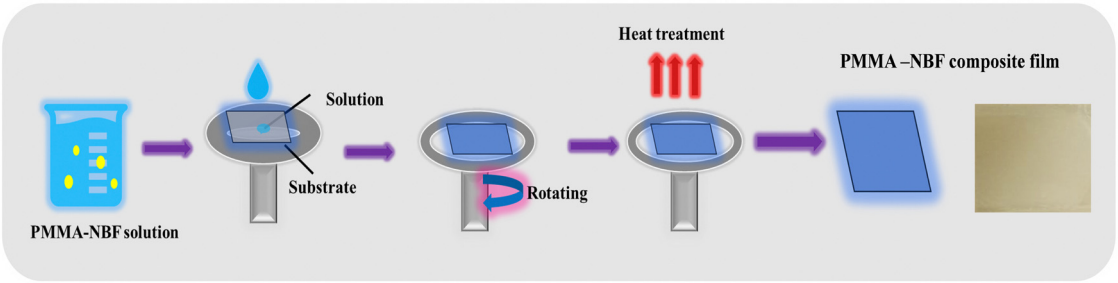

Scheme 1 Fabrication of PMMA–NBF:Gd/Tb composite films.

traps (E-traps) and hole traps (H-traps), respectively. The secondary electrons captured by E-traps can escape over time to the conduction band followed by their migration to the activators; meanwhile, the trapped holes can also migrate toward the activators, leading to radiative emission *via* electron–hole recombination. For $NaBiF_4$:20Gd/20Tb NPs, a significant portion of Bi^{3+} ions in the matrix facilitates energy migration from E-trap states to surface quenchers *via* the Bi^{3+} sublattice, reducing electron storage in the E-trap states and resulting in a substantial afterglow reduction. Additionally, the Gd^{3+} excited state competes with E-trap states for capturing secondary electrons, leading to a decreased electron population in the E-trap states and a subsequent reduction in afterglow (Fig. S8(c), ESI†).

The integral scintillation intensity of the NBF:20Gd/20Tb NSs was measured to be about 37.8% of that from the commercial CsI (Tl), which is much higher than the previously reported value of 11.5% [Fig. S8(b), ESI†]. The stability tests of the NBF:20Gd/20Tb NPs were conducted under continuous X-ray irradiation (Fig. S8(d), ESI†). The radioluminescence intensities of the NBF:20Gd/20Tb NPs show no obvious reduction after continuous X-ray exposure for 60 min, indicating excellent resistance to X-ray radiation damage [Fig. S8(d), ESI†].

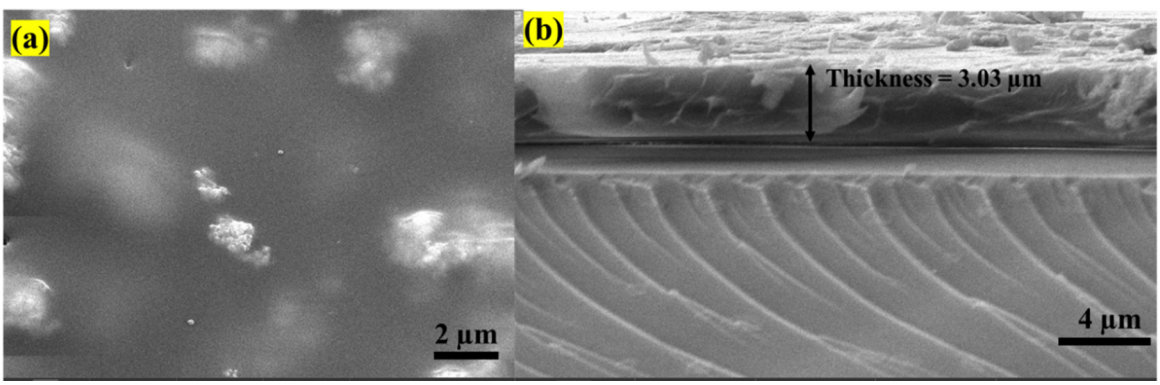

Fig. 7 (a) FESEM image of a PMMA–NBF film and (b) cross-sectional FE-SEM image of a PMMA–NBF thin film.

To explore the potential application of these NSs in X-ray imaging, uniform PMMA–NBF composite films were prepared. A uniform film with a thickness of ~3.03 μm was prepared by blending NBF:20Gd/20Tb NPs with PMMA (Fig. 7(b)). The FE-SEM (Fig. 7(a)) and EDX images indicate uniformity and the presence of all the elements in the film (Fig. S9, ESI†). More importantly, this film is highly transparent in the measured wavelengths ranging from 400 to 700 nm (Fig. 8(b)), benefiting from the reduced light scattering and then a reduction in the signal cross-talk in the photodiode array, thus producing an improved image resolution. For application in radiography, it is important to optically characterize the NBF:Gd/Tb nanoparticles as well as the PMMA–NBF composite films.

The optical characterization was carried out by recording the absorption spectra and the photoluminescence spectra. The absorption spectra of the NBF:Gd/Tb and PMMA–NBF:Gd/Tb composite films are compared in Fig. S8(a) (ESI†). All the samples exhibit absorption bands at 368, 377, and 486 nm, which can be attributed to the Tb^{3+} $^7F_6 \rightarrow {}^5L_{10}$, $^5D_3$, $^5D_4$ transitions. Whereas, the bands peaking at ~275 and ~225 nm belong to the low spin-allowed (LS) 4f → $5d_1$ and 4f → $5d_2$ absorption transitions, respectively, in Tb^{3+}. It is clear that there are additional peaks at about 250, 273, and 312 nm, which are assigned to the Gd^{3+} transitions from the ground level $^8S_{7/2}$ to excited levels ^6D_J, ^6I_J, ^6P_J, respectively. No additional bands were observed due to PMMA.[42] The comparison between the absorption spectra of the PMMA–NBF:Gd/Tb composite films with varying thickness is shown in Fig. 8(a). No significant change in absorbance is observed with varying thickness of the film, indicating that the PMMA matrix is transparent to NBF:Gd/Tb emission and this confirms that thicker films can be used as imaging screens.

Fig. S10(a) (ESI†) shows the transmittance spectra of the prepared PMMA:NBF films with different thicknesses, 3 and 6 μm. It is observed that with an increase in the thickness of the PMMA:NBF film the transmittance was decreased and the corresponding image quality (resolution) became worse due to the increased light scattering from the NBF particles (Fig. S10(b), ESI†).

Fig. 8(c) shows the PL spectra of the PMMA–NBF:Gd/Tb composite film. The emission spectra of the composite films consist of an intense peak at 544 nm. This emission is due to

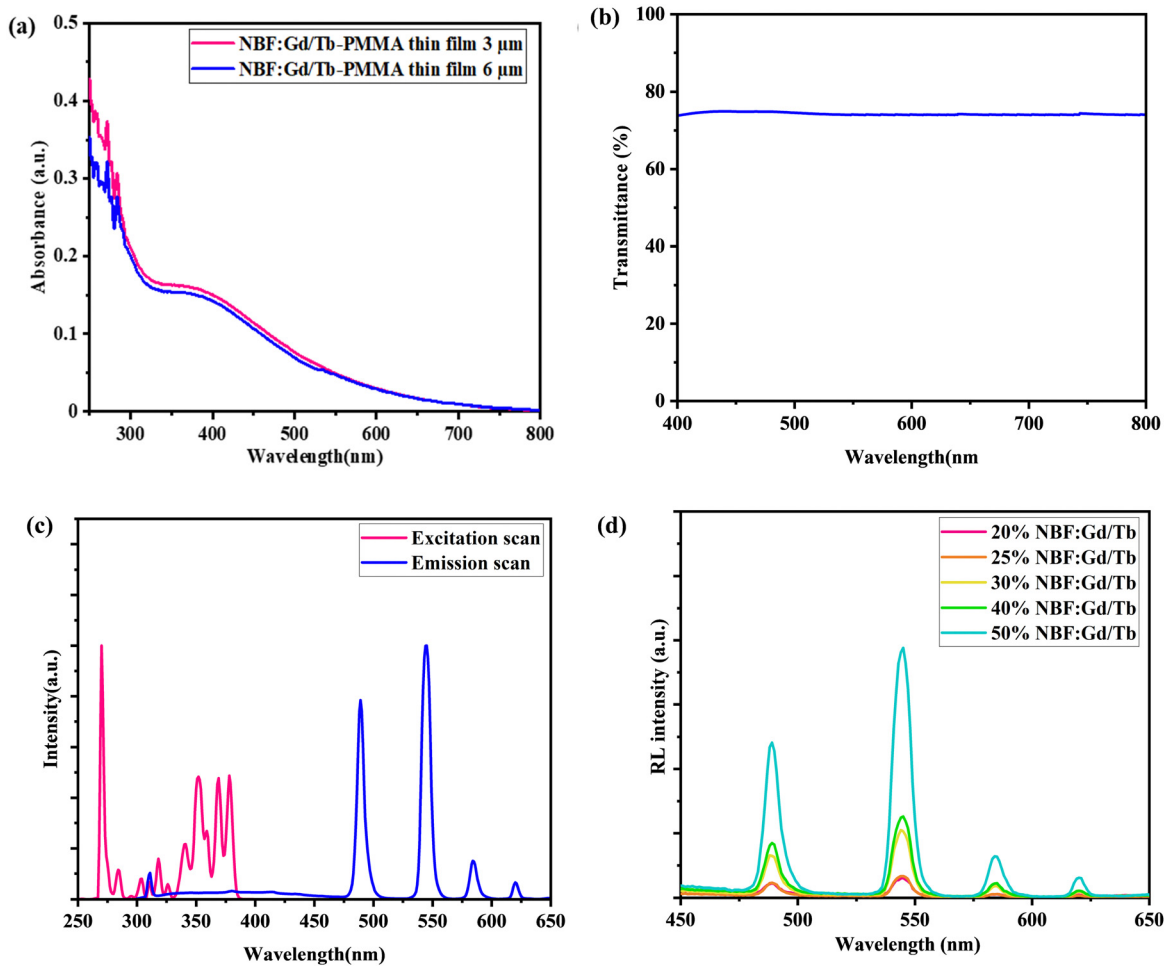

Fig. 8 (a) Absorption spectra of PMMA–NBF films of thickness 3 and 6 μm; (b) transmission spectra of the PMMA–NBF film; (c) excitation and PL spectra of the PMMA–NBF film; (d) XEOL spectra of PMMA–NBF with different loading percentages.

the $^5D_4 \rightarrow {}^7F_5$ transitions of Tb^{3+} ions present in the NBF lattice.[18] This confirms that the luminescence property of the composite film is dominated by the inorganic component (NBF:Gd/Tb) and the organic polymer is transparent to this emission and it does not give any additional emission, nor does it affect the luminescence properties of NBF:Gd/Tb. The advantage of the green emission at 544 nm is that it can be directly coupled to a CCD camera that has its maximum sensitivity in this range for imaging applications.

The scintillation and PL properties of the PMMA–NBF composite films were evaluated by measuring their luminescence characteristics. The main RL peak observed at 544 nm (Fig. 8(d)) closely resembles the PL peak and hence can be attributed to the Tb emission. The integrated XEOL intensity of the NBF:Gd/Tb as a function of X-ray tube voltage and tube current is shown in (Fig. 9(a) and (b)). An increase in the integrated RL intensity is observed initially with increasing voltage and then it starts saturating. The integrated XEOL intensity is linearly correlated with X-ray dose, which is in favour of high X-ray image contrast [Fig. 9(c) and (d)].

Fig. 8(d) shows the XEOL spectra of PMMA:NBF composite films at different loading percentages. XEOL spectra for all the films show peaks at 490, 544, 590 and 621 nm and are attributed to the $^5D_4 \rightarrow {}^7F_6$, $^5D_4 \rightarrow {}^7F_5$, $^5D_4 \rightarrow {}^7F_4$, and $^5D_4 \rightarrow {}^7F_3$, transitions, respectively, of Tb^{3+} ions present in the NBF lattice.[18] The XEOL and PL (Fig. S11(a), ESI†) intensity increases on increasing the loading level of NBF due to the presence of more luminescent centres. Fig. S11(b) (ESI†) shows the transmission spectra of the PMMA:NBF film (thickness 3 μm) with different loading percentages. It is observed that with an increase in the loading percentage the transmittance decreases due to the increased scattering from the NBF particles.

Considering the requirements for high-quality X-ray imaging and high-sensitivity photoelectric conversion, strong RL and high transparency of PMMA–NBF:Gd,Tb composite films are expected. Therefore, the PMMA–NBF:Gd,Tb composite film was selected to demonstrate their practical application.

To further reveal the potential possibility of our prepared NBF:20Gd/20Tb nanoscintillator for practical X-ray imaging, its corresponding uniform film is employed as a nanoscintillator screen and a simple X-ray imaging system is setup (Fig. 10). The composite film was kept at the screen position and a direct image of the X-ray beam as well as the image shadow of the duplex wire was recorded using a commercially available CCD camera in the transmission mode. Fig. S12 (ESI†) shows the X-ray images recorded with PMMA:NBF (thickness 3 μm) films

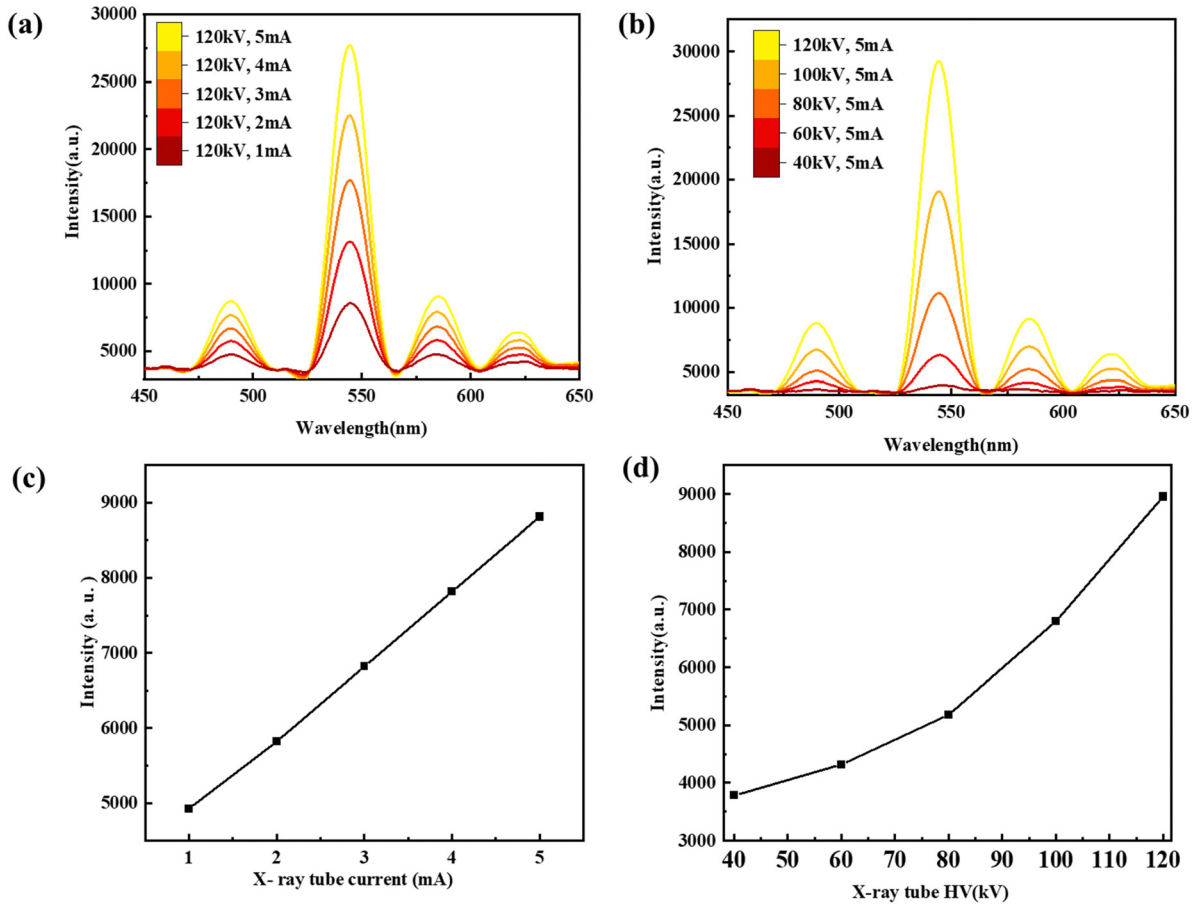

Fig. 9 Radioluminescence spectra of (a) NBF:Gd/Tb exposed to varied X-ray tube currents and (b) NBF:Gd/Tb film under varied X-ray tube voltages, (c) NBF:Gd/Tb integrated RL intensity as a function of varying tube current at constant tube voltage and (d) NBF:Gd/Tb integrated RL intensity as a function of varying tube voltages at constant current.

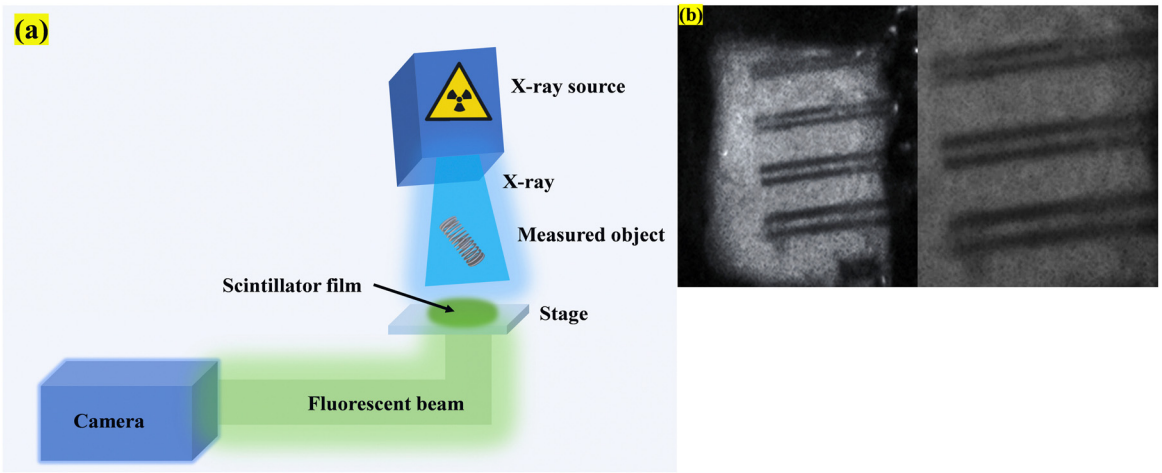

Fig. 10 (a) X-Ray radiography setup consisting of an X-ray source, object, CCD camera, and the composite screen and (b) image formed by a duplex wire with a resolution of 100 microns.

with different loading percentages. We observe that the brightness and the sharpness of the image increase with the loading from 20 to 50% (amount of NBF:Gd/Tb is 20% "by weight" to that of PMMA polymer). The best image is recorded for a 50% loaded film. As stated earlier, increasing the loading percentage of NBF beyond 50% also rendered brittleness to the films and generation of stress, which makes the films curl at the edges. The best results have been achieved in 50% loading (amount of $NaBiF_4$: 20Gd/20Tb is 50% "by weight" to that of the PMMA polymer). A spatial resolution of 100 microns was achieved with the PMMA–NBF composite film using the standard line pair (Fig. 10(b)). The radiography image is of a duplex wire, imaged successfully by a PMMA–NBF-50 composite film with a spatial resolution of 100 microns (10 lp mm^{-1}). We would like to add that this value is comparable to that for typical commercial CsI (Tl) scintillator[40] ($\sim$10 lp mm^{-1})-based X-ray imaging and much better than the resolution of 2.8 lines per mm reported for commercial Gd_2O_2S:Tb, GOS:Tb screens.[41,42,44]

4. Conclusions

In summary, NBF:20Gd/20Tb NP was synthesized using the co-precipitation method at room temperature. These NSs showed strong XEOL intensity, excellent stability, and ultra-weak afterglow. The incorporation of Gd^{3+} ions enhanced the XEOL intensity of the $NaBiF_4$:Tb NSs, indicating energy transfer from Gd^{3+} to Tb^{3+} ions. Moreover, by employing the highly transparent NBF:20Gd/20Tb film with a thickness of 3.03 μm as a nanoscintillator screen for XEOL imaging, a high spatial resolution of 100 microns was realized, which is comparable to the commercial CsI (TI) scintillator and much better than that of the commercial Gd_2O_2S:Tb, GOS:Tb scintillators employed for screens. Our results promote the development of a new generation of NSs, with low cost and high performance in the X-ray imaging field. Overall, this work represents a new direction for designing and developing Bi-based nanophosphors for rare earth luminescence upon X-ray excitation, and will lead the way to access broad use of these advanced bismuth-based NSs for X-ray detection and imaging applications.

Conflicts of interest

The authors declare no competing financial interest.

Acknowledgements

A. K. G. thanks the Department of Science & Technology (DST), Govt. of India for providing financial support. M. B. thanks CSIR and University at Buffalo for the support. We acknowledge Dr P. S. Sarkar from Technical Physics Division, BARC for his support in the measurement of X-ray imaging.

References

1 H. Wu, Q. Wang, A. Zhang, G. Niu, M. Nikl, C. Ming, J. Zhu, Z. Zhou, Y. Y. Sun, G. Nan, G. Ren, Y. Wu and J. Tang, One-Dimensional Scintillator Film with Benign Grain Boundaries for High-Resolution and Fast X-ray Imaging, *Sci. Adv.*, 2023, **9**, DOI: 10.1126/sciadv.adh1789.
2 S. Y. Yao, H. Li, M. Zhou, T. C. Wang, X. Yu, Y. S. Xu, J. H. Yi, J. B. Qiu, J. Yu and X. H. Xu, Visualization of X-Rays with an Ultralow Detection Limit via Zero-Dimensional Perovskite Scintillators, *ACS Appl. Mater. Interfaces*, 2022, **14**, 56957–56962.
3 T.-C. Wang, S.-Y. Yao, S.-P. Yan, J. Yu, Z.-Y. Deng, A. N. Yakovlev, B. Meng, J.-B. Qiu and X.-H. Xu, High Thermal Stability of Copper-Based Perovskite Scintillators for High-Temperature X-Ray Detection, *ACS Appl. Mater. Interfaces*, 2023, **15**, 23421–23428.
4 L. Lian, M. Zheng, W. Zhang, L. Yin, X. Du, P. Zhang, X. Zhang, J. Gao, D. Zhang, L. Gao, G. Niu, H. Song, R. Chen, X. Lan, J. Tang and J. Zhang, Efficient and Reabsorption-Free Radioluminescence in $Cs_3Cu_2I_5$ Nanocrystals with Self-Trapped Excitons, *Adv. Sci.*, 2020, **7**, 2000195.

5 X. Wang, H. Shi, H. Ma, W. Ye, L. Song, J. Zan, X. Yao, X. Ou, G. Yang, Z. Zhao, M. Singh, C. Lin, H. Wang, W. Jia, Q. Wang, J. Zhi, C. Dong, X. Jiang, Y. Tang, X. Xie, Y. Yang, J. Wang, Q. Chen, Y. Wang, H. Yang, G. Zhang, Z. An, X. Liu and W. Huang, Organic Phosphors with Bright Triplet Excitons for Efficient X-Ray-Excited Luminescence, *Nat. Photonics*, 2021, **15**, 187–192.

6 T. Ji, T. Wang, H. Li, Q. Peng, H. Tang, S. Hu, A. Yakovlev, Y. Zhong and X. Xu, Ce^{3+}-Doped Yttrium Aluminum Garnet Transparent Ceramics for High-Resolution X-Ray Imaging, *Adv. Opt. Mater.*, 2022, **10**, 2102056.

7 J. Ma, W. Zhu, L. Lei, D. Deng, Y. Hua, Y. M. Yang, S. Xu and P. N. Prasad, Highly Efficient $NaGdF_4$:Ce/Tb Nanoscintillator with Reduced Afterglow and Light Scattering for High-Resolution X-Ray Imaging, *ACS Appl. Mater. Interfaces*, 2021, **13**, 44596–44603.

8 Y. C. Kim, K. H. Kim, D.-Y. Son, D.-N. Jeong, J.-Y. Seo, Y. S. Choi, I. T. Han, S. Y. Lee and N.-G. Park, Printable Organometallic Perovskite Enables Large-Area, Low-Dose X-Ray Imaging, *Nature*, 2017, **550**, 87–91.

9 W. Ma, Y. Su, Q. Zhang, C. Deng, L. Pasquali, W. Zhu, Y. Tian, P. Ran, Z. Chen, G. Yang, G. Liang, T. Liu, H. Zhu, P. Huang, H. Zhong, K. Wang, S. Peng, J. Xia, H. Liu, X. Liu and Y. (Michael) Yang, Thermally Activated Delayed Fluorescence (TADF) Organic Molecules for Efficient X-Ray Scintillation and Imaging, *Nat. Mater.*, 2022, **21**, 210–216.

10 Y. Zhang, Light People: Professor Jianhua Jiang, *Light: Sci. Appl.*, 2022, **11**, 12.

11 L.-J. Xu, X. Lin, Q. He, M. Worku and B. Ma, Highly Efficient Eco-Friendly X-Ray Scintillators Based on an Organic Manganese Halide, *Nat. Commun.*, 2020, **11**, 4329.

12 I. V. Khodyuk, P. A. Rodnyi and P. Dorenbos, Nonproportional Scintillation Response of NaI:Tl to Low Energy X-Ray Photons and Electrons, *J. Appl. Phys.*, 2010, **107**, 113513.

13 W. Ma, T. Jiang, Z. Yang, H. Zhang, Y. Su, Z. Chen, X. Chen, Y. Ma, W. Zhu, X. Yu, H. Zhu, J. Qiu, X. Liu, X. Xu and Y. (Michael) Yang, Highly Resolved and Robust Dynamic X-Ray Imaging Using Perovskite Glass-Ceramic Scintillator with Reduced Light Scattering, *Adv. Sci.*, 2021, **8**, 2003728.

14 E. Dieguez, L. Arizmendi and J. M. Cabrera, X-Ray Induced Luminescence, Photoluminescence and Thermoluminescence of Bi4Ge3O12, *J. Phys. C: Solid State Phys.*, 1985, **18**, 4777–4783.

15 J. K. Chen, N. Shirahata and H. T. Sun, Metal-free scintillators excite X-ray community, *Nat. Photonics*, 2021, **15**, 171–172.

16 Q. Chen, J. Wu and X. Ou, *et al.*, All-inorganic perovskite nanocrystal scintillators, *Nature*, 2018, **561**, 88–93.

17 H. Chen, X. Sun, G. D. Wang, K. Nagata, Z. Hao, A. Wang, Z. Li, J. Xie and B. Shen, $LiGa_5O_8$:Cr-Based Theranostic Nanoparticles for Imaging-Guided X-Ray Induced Photodynamic Therapy of Deep-Seated Tumors, *Mater. Horiz.*, 2017, **4**, 1092–1101.

18 R. Yasuda, M. Kataigiri and M. Matsubayashi, Influence of powder particle size and scintillator layer thickness on the performance of Gd_2O_2S:Tb scintillators for neutron imaging, *Nucl. Instrum. Methods Phys. Res., Sect. A*, 2012, **680**, 139–144.

19 B. Yang, L. X. Yin, G. D. Niu, J. H. Yuan, K. H. Xue, Z. F. Tan, X. S. Miao, M. Niu, X. Du, H. S. Song, E. Lifshitz and J. Tang, Lead-Free Halide Rb_2CuBr_3 as Sensitive X-Ray Scintillator, *Adv. Mater.*, 2019, **31**, 1904711.

20 T. Jiang, Z. Chen, X. Chen, X. Chen, X. Xu, T. Liu, L. Bai, D. Yang, D. Di, W. E. I. Sha, H. Zhu and Y. M. Yang, Power Conversion Efficiency Enhancement of Low-Bandgap Mixed Pb–Sn Perovskite Solar Cells by Improved Interfacial Charge Transfer, *ACS Energy Lett.*, 2019, **4**, 1784–1790.

21 T. Jiang, Z. Chen, X. Chen, T. Liu, X. Chen, W. E. I. Sha, H. Zhu and Y. (Michael) Yang, Realizing High Efficiency over 20% of Low-Bandgap Pb–Sn-Alloyed Perovskite Solar Cells by In Situ Reduction of Sn^{4+}, *Sol. RRL*, 2020, **4**, 1900467.

22 Y. Gao, Z. Wei, P. Yoo, E. Shi, M. Zeller, C. Zhu, P. Liao and L. Dou, Highly Stable Lead-Free Perovskite Field-Effect Transistors Incorporating Linear π-Conjugated Organic Ligands, *J. Am. Chem. Soc.*, 2019, **141**, 15577–15585.

23 J. Qiu, H. Zhao, Z. Mu, J. Chen, H. Gu, C. Gu, G. Xing, X. Qin and X. Liu, Turning Nonemissive $CsPb_2Br_5$ Crystals into High-Performance Scintillators through Alkali Metal Doping, *Nano Lett.*, 2024, **24**, 2503–2510.

24 F. Wang and X. Liu, Upconversion Multicolor Fine-Tuning: Visible to Near-Infrared Emission from Lanthanide-Doped $NaYF_4$ Nanoparticles, *J. Am. Chem. Soc.*, 2008, **130**, 5642–5643.

25 P. Huang, W. Zheng, S. Zhou, D. Tu, Z. Chen, H. Zhu, R. Li, E. Ma, M. Huang and X. Chen, Lanthanide-Doped $LiLuF_4$ Upconversion Nanoprobes for the Detection of Disease Biomarkers, *Angew. Chem., Int. Ed.*, 2014, **53**, 1252–1257.

26 L. Lei, Y. Wang, W. Xu, R. Ye, Y. Hua, D. Deng, L. Chen, P. N. Prasad and S. Xu, Manipulation of time-dependent multicolour evolution of X-ray excited afterglow in lanthanide-doped fluoride nanoparticles, *Nat. Commun.*, 2022, **13**, 5739.

27 L. Lei, Y. Wang, A. Kuzmin, Y. Hua, J. Zhao, S. Xu and P. N. Prasad, Next generation lanthanide doped nanoscintillators and photon converters, *eLight*, 2022, **2**, 17.

28 L. Lei, M. Yi, Y. Wang, Y. Hua, J. Zhang, P. N. Prasad and S. Xu, Dual heterogeneous interfaces enhance X-ray excited persistent luminescence for low-dose 3D imaging, *Nat. Commun.*, 2024, **15**, 1140.

29 H. H. Gorris and O. S. Wolfbeis, Photon-Upconverting Nanoparticles for Optical Encoding and Multiplexing of Cells, Biomolecules, and Microspheres, *Angew. Chem., Int. Ed.*, 2013, **52**, 3584–3600.

30 J. Zhou, Q. Liu, W. Feng, Y. Sun and F. Li, Upconversion Luminescent Materials: Advances and Applications, *Chem. Rev.*, 2015, **115**, 395–465.

31 M. Bungla, P. Sharma, A. Shanavas and A. K. Ganguli, Methylene blue loaded $K_{0.3}Bi_{0.7}F_{2.4}$:Yb,Er upconversion nanoparticles for near-infrared activated photodynamic therapy, *New J. Chem.*, 2024, **48**, 1800–1808.

32 D. Chen, Y. Liang, S. Miao, X. Shan, X. Wang, W. Wang, Y. Zhang, J. Bi and D. Tang, Self-surfactant room-

temperature synthesis of morphology-controlled $K_{0.3}Bi_{0.7}F_{2.4}$ nanoscintillators, *J. Mater. Chem. C*, 2022, **10**, 14296–14305.

33 Y. Guo, J. Xie, M. Yu, W. Huang, H. Yang, X. Li, L. Wang and Q. Zhang, The enhanced up-conversion green by Yb–Mn dimer in $NaBiF_4$:Yb^{3+}/Er^{3+}/Mn^{2+} for optical fiber temperature sensor, *J. Alloys Compd.*, 2021, **888**, 161497.

34 X. Gao, D. Ju, X. Sang, J. Yang, Y. Zhang and F. Song, Temperature-responsive $NaBiF_4$:Yb^{3+},Er^{3+}/Tm^{3+} based on non-thermally coupled levels, *J. Lumin.*, 2023, **257**, 119711.

35 L. Sun, $NaBiF_4$-based hollow upconversion nanoparticles for temperature sensing, *Light: Sci. Appl.*, 2022, **11**, 257.

36 X. Zhang, J. Chen, Y. Min, G. B. Park, X. Shen, S. Song, Y. Sun, H. Wang, W. Long, J. Xie, K. Gao, L. Zhang, S. Fan, F. Fan and U. Jeong, Metabolizable Bi_2Se_3 Nanoplates: Biodistribution, Toxicity, and Uses for Cancer Radiation Therapy and Imaging, *Adv. Funct. Mater.*, 2014, **24**, 1718–1729.

37 P. Lei, R. An, X. Zhai, S. Yao, L. Dong, X. Xu, K. Du, M. Zhang, J. Feng and H. Zhang, Benefits of Surfactant Effects on Quantum Efficiency Enhancement and Temperature Sensing Behavior of $NaBiF_4$ Upconversion Nanoparticles, *J. Mater. Chem. C*, 2017, **5**, 9659–9665.

38 M. Bungla, S. Chowdhari, M. Shanu, P. Pragya, V. Perumal, G. V. Prakash and A. K. Ganguli, $NaBiF_4$:Yb^{3+},Tm^{3+} Submicron Particles as Luminescent Probes for in Vitro Imaging of Cells, *Phys. Chem. Chem. Phys.*, 2023, **25**, 6131–6141.

39 P. Lei, R. An, S. Yao, Q. Wang, L. Dong, X. Xu, K. Du, J. Feng and H. Zhang, Ultrafast Synthesis of Novel Hexagonal Phase $NaBiF_4$ Upconversion Nanoparticles at Room Temperature, *Adv. Mater.*, 2017, **29**, 1700505.

40 J. H. Heo, D. H. Shin, J. K. Park, D. H. Kim, S. J. Lee and S. H. Im, High-Performance Next-Generation Perovskite Nanocrystal Scintillator for Nondestructive X-Ray Imaging, *Adv. Mater.*, 2018, **30**, DOI: **10.1002/adma.201801743**.

41 P. Büchele, M. Richter, S. F. Tedde, G. J. Matt, G. N. Ankah, R. Fischer, M. Biele, W. Metzger, S. Lilliu, O. Bikondoa, J. E. Macdonald, C. J. Brabec, T. Kraus, U. Lemmer and O. Schmidt, X-Ray Imaging with Scintillator-Sensitized Hybrid Organic Photodetectors, *Nat. Photonics*, 2015, **9**, 843–848.

42 P. Du, Y. Hua and J. S. Yu, Room-temperature synthesis of near-ultraviolet light-excited Tb^{3+}-doped $NaBiF_4$ green-emitting nanoparticles for solid-state lighting, *RSC Adv.*, 2018, **8**, 26676–26681.

43 R. An, P. Lei, P. Zhang, X. Xu, J. Feng and H. Zhang, Near-infrared optical and X-ray computed tomography dual-modal imaging probe based on novel lanthanide-doped $K_{0.3}Bi_{0.7}F_{2.4}$ upconversion nanoparticles, *Nanoscale*, 2018, **10**, 1394–1402.

44 L. Chen, Y. Wu, H. Huo, B. Tang, X. Ma, J. Wang, C. Sun, J. Sun and S. Zhou, Nanoscale Gd_2O_2S:Tb Scintillators for High-Resolution Fluorescent Imaging of Cold Neutrons, *ACS Appl. Nano Mater.*, 2022, **5**, 8440–8447.